Title

An allelic series of miR-17~92–mutant mice uncovers functional specialization and cooperation among members of a microRNA polycistron

Journal

Nature Genetics, 47(7)

ISSN

1061-4036

Authors

Han, Yoon-Chi
Vidigal, Joana A
Mu, Ping
et al.

Publication Date

2015-07-01

DOI

10.1038/ng.3321

Peer reviewed

nature genetics

An allelic series of miR-17~92–mutant mice uncovers functional specialization and cooperation among members of a microRNA polycistron

Yoon-Chi Han[1,2,10], Joana A Vidigal[1,10], Ping Mu[1,3,10], Evelyn Yao[1,3], Irtisha Singh[4], Alvaro J González[4], Carla P Concepcion[1,3], Ciro Bonetti[1], Paul Ogrodowski[1], Brett Carver[5,6], Licia Selleri[7], Doron Betel[8,9], Christina Leslie[4] & Andrea Ventura[1]

Polycistronic microRNA (miRNA) clusters are a common feature of vertebrate genomes. The coordinated expression of miRNAs belonging to different seed families from a single transcriptional unit suggests functional cooperation, but this hypothesis has not been experimentally tested. Here we report the characterization of an allelic series of genetically engineered mice harboring selective targeted deletions of individual components of the miR-17~92 cluster. Our results demonstrate the coexistence of functional cooperation and specialization among members of this cluster, identify a previously undescribed function for the miR-17 seed family in controlling axial patterning in vertebrates and show that loss of miR-19 selectively impairs Myc-driven tumorigenesis in two models of human cancer. By integrating phenotypic analysis and gene expression profiling, we provide a genome-wide view of how the components of a polycistronic miRNA cluster affect gene expression *in vivo*. The reagents and data sets reported here will accelerate exploration of the complex biological functions of this important miRNA cluster.

miRNAs modulate gene expression at the post-transcriptional level by repressing translation and by promoting destabilization of target mRNAs[1–4]. Target specificity is largely dictated by nucleotides at positions 2–7 of the miRNA (the 'seed'), and miRNAs with the same seed sequence can be grouped into 'seed families' (ref. 1). Approximately 60% of mammalian miRNAs are part of polycistronic clusters, and in many cases multiple seed families are represented within a single polycistron[5]. Coordinated expression of unrelated miRNAs from the same transcription unit could provide a simple mechanism for different miRNAs to act cooperatively, thus explaining why this gene structure has been so frequently favored by natural selection. To test this hypothesis, we investigated the miR-17~92 cluster, a classic polycistronic miRNA gene with essential roles in development and disease[6].

miR-17~92 (also called *Mirc1* in mice) consists of six highly conserved miRNAs belonging to four seed families (**Fig. 1a**). In mice, targeted deletion of the whole cluster causes a wide array of developmental defects affecting multiple organs and systems[7], whereas, in humans, germline monoallelic microdeletions involving miR-17~92 are responsible for the developmental defects observed in a subset of individuals with Feingold syndrome[8] (FS2; MIM 614326), an autosomal dominant disease characterized by short stature and variable combinations of craniofacial abnormalities, limb and digit malformations, gastrointestinal atresia and learning disabilities[9].

The miR-17~92 cluster is also a bona fide human oncogene. Focal amplifications of its locus are frequent in human diffuse large B cell lymphomas[10], and its components are overexpressed in many human cancers[11–16], at least partially as a result of direct transcriptional activation by members of the Myc family of oncogenic transcription factors[17]. In addition, ectopic expression of miR-17~92 accelerates or initiates tumor formation in several mouse models of human cancer[12,18–24].

We reasoned that the multiple phenotypes caused by miR-17~92 deletion could be used to experimentally determine the extent of functional cooperation among the miRNAs encoded by a polycistronic cluster. Here we report the generation of an allelic series of miR-17~92–mutant mice and integrate their phenotypic characterization with RNA sequencing (RNA-seq) analysis showing the consequences of selective miRNA inactivation on gene expression in the developing embryo. Our results provide new insights into the biology of this important oncogenic miRNA cluster and pave the way for further mechanistic studies.

[1]Cancer Biology and Genetics Program, Memorial Sloan Kettering Cancer Center, New York, New York, USA. [2]Oncology Research Unit, Pfizer, Inc., Pearl River, New York, USA. [3]Weill Cornell Graduate School of Medical Sciences of Cornell University, New York, New York, USA. [4]Computational Biology Program, Memorial Sloan Kettering Cancer Center, New York, New York, USA. [5]Human Oncology and Pathogenesis Program. Memorial Sloan Kettering Cancer Center, New York, New York, USA. [6]Department of Surgery, Memorial Sloan Kettering Cancer Center, New York, New York, USA. [7]Department of Cell and Developmental Biology, Weill Cornell Medical College, New York, New York, USA. [8]Division of Hematology and Medical Oncology, Department of Medicine, Weill Cornell Medical College, New York, New York, USA. [9]Institute for Computational Biomedicine, Weill Cornell Medical College, New York, New York, USA. [10]These authors contributed equally to this work. Correspondence should be addressed to A.V. (venturaa@mskcc.org).

Received 26 November 2014; accepted 4 May 2015; published online 1 June 2015; doi:10.1038/ng.3321

RESULTS

Generation of an allelic series of miR-17~92 deletions

We used homologous recombination in mouse embryonic stem (ES) cells to generate six miR-17~92 alleles (**Fig. 1b** and **Supplementary Fig. 1a**), each characterized by the deletion of genomic sequences corresponding to one or more of its pre-miRNAs. Four alleles harbored deletion of the components of single-seed families: miR-17~92$^{\Delta 17}$ (deletion of *Mir17* and *Mir20a*), miR-17~92$^{\Delta 18}$ (deletion of *Mir18*), miR-17~92$^{\Delta 19}$ (deletion of *Mir19a* and *Mir19b-1*) and miR-17~92$^{\Delta 92}$ (deletion of *Mir92-1*). Two additional alleles, miR-17~92$^{\Delta 17,18}$ (deletion of *Mir17*, *Mir20a* and *Mir18*) and miR-17~92$^{\Delta 17,18,92}$ (deletion of *Mir17*, *Mir20a*, *Mir18* and *Mir92-1*) are characterized by targeted deletion of more than one seed family. The miR-17~92$^{\Delta 17,18}$ allele was generated because members of the miR-17 and miR-18 seed families have high sequence homology and their seeds differ only at position 4. Finally, the miR-17~92$^{\Delta 17,18,92}$ allele retains only pre-miRNAs belonging to the miR-19 family, and its generation was prompted by reports indicating that this seed family is the key oncogenic determinant of the cluster[21,25,26]. After germline transmission of the targeted alleles, we intercrossed heterozygous mice to generate homozygous-mutant mice for each allele of the series (**Table 1**).

We confirmed loss of expression of the deleted miRNAs in homozygous mice by both reverse transcription coupled with quantitative PCR (RT-qPCR) and small-RNA sequencing (**Fig. 1c** and **Supplementary Fig. 1b**,**c**). For each allele, we found that the expression of the remaining miRNAs was not substantially altered, with the notable exception of a substantial reduction in miR-18 levels in miR-17~92$^{\Delta 17/\Delta 17}$ mice. Expression profiling of wild-type and mutant mice, however, suggested that this reduction has very limited, if any, functional consequences (**Supplementary Note**). Finally, no changes in the sequences of the mature miRNAs encoded by the various miR-17~92 alleles were detected by small-RNA sequencing (data not shown).

Perinatal lethality, cardiac defects and lung hypoplasia

Homozygous deletion of the miR-17~92 cluster results in fully penetrant perinatal lethality, a phenotype that has been attributed to severe lung hypoplasia and defective cardiac development[7] (**Table 1** and **Supplementary Fig. 2**). By contrast, heterozygous intercrosses of the single-seed mutants yielded viable homozygous adults at expected mendelian ratios, and even combined deletion of the miR-17 and miR-18 seed families was compatible with postnatal survival. For each of the strains, crosses between homozygous mice produced viable offspring (data not shown). Strikingly, we observed perinatal lethality only in miR-17~92$^{\Delta 17,18,92/\Delta 17,18,92}$ mice (**Table 1**), and only these mice displayed lung hypoplasia (**Supplementary Fig. 2**). Defective heart development was only detected upon deletion of the entire cluster (**Supplementary Fig. 2**). Thus, the perinatal lethality, cardiac defects and lung hypoplasia observed in miR-17~92–null mice result from the concomitant loss of multiple components of the cluster, providing a clear example of functional cooperation.

Although the characterization of miR-17~92–null mice[7] and the analysis described above were performed on mice of a mixed B6-129 background, we observed during this study that backcrossing the mutant alleles into a pure C57BL/6J genetic background

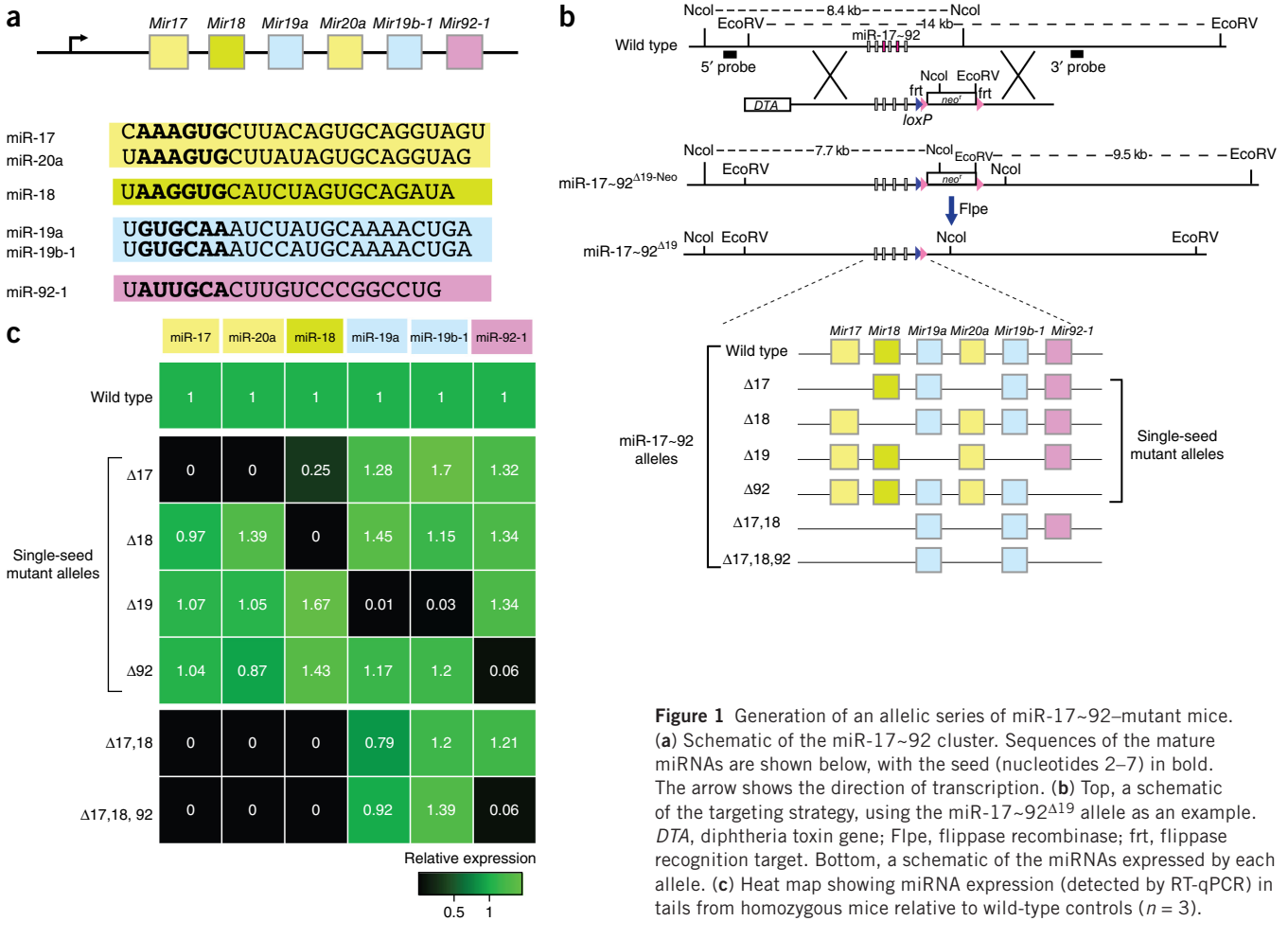

Figure 1 Generation of an allelic series of miR-17~92–mutant mice. (**a**) Schematic of the miR-17~92 cluster. Sequences of the mature miRNAs are shown below, with the seed (nucleotides 2–7) in bold. The arrow shows the direction of transcription. (**b**) Top, a schematic of the targeting strategy, using the miR-17~92$^{\Delta 19}$ allele as an example. *DTA*, diphtheria toxin gene; Flpe, flippase recombinase; frt, flippase recognition target. Bottom, a schematic of the miRNAs expressed by each allele. (**c**) Heat map showing miRNA expression (detected by RT-qPCR) in tails from homozygous mice relative to wild-type controls ($n = 3$).

Table 1 Absolute numbers and frequencies of genotypes obtained from heterozygous breeding

miR-17~92 allele	+/+ (25% expected)	Δ/+ (50% expected)	Δ/Δ (25% expected)	Corrected *P*
Δ17	38/105 (36%)	49/105 (46%)	18/105 (18%)	NS
Δ18	29/111 (26%)	42/111 (38%)	40/111 (36%)	NS
Δ19	32/109 (29%)	54/109 (50%)	23/109 (21%)	NS
Δ92	28/125 (22%)	61/125 (49%)	36/125 (29%)	NS
Δ17,18	33/94 (35%)	46/94 (49%)	15/94 (16%)	NS
Δ17,18,92	49/106 (46%)	57/106 (54%)	0/106 (0%)	<0.0005
Δ17,18,92 (P0)	19/73 (26%)	33/73 (45%)	21/73 (28%)	NS
Δ17~92(Δ)	101/240 (42%)	139/240 (58%)	0/240 (0%)	<0.0005

P values are from an adjusted χ^2 test comparing the observed and expected frequencies. Genotypes were determined on postnatal days (P) 10–12, except for the miR-17~92$^{\Delta 17,18,92}$ allele, for which mice were also examined at birth (P0). NS, not significant.

resulted in generally more severe phenotypes. More specifically, we noticed that a smaller fraction of miR-17~92$^{\Delta/\Delta}$ embryos (embryos harboring homozygous deletion of the entire miRNA cluster) reached full term, and we observed substantial perinatal lethality in mice harboring deletion of members of the miR-17 or miR-19 seed families (**Supplementary Table 1**).

Feingold syndrome and axial patterning

Hemizygosity at the miR-17~92 locus in mice phenocopies several of the key features of FS2, including size and digit abnormalities[8]. To define the relative contribution of each seed family to the pathogenesis of this syndrome, we examined mice from the miR-17~92 allelic series. Homozygous mice for each of the four single-seed mutant alleles were smaller than age- and sex-matched wild-type controls (**Fig. 2a**,**b**). This phenotype was most severe in miR-17~92$^{\Delta 17/\Delta 17}$ mice, which at 5 weeks of age weighed on average 40% less than wild-type mice ($P = 7.47 \times 10^{-7}$, two-tailed *t* test). Co-deletion of the miR-17 and miR-18 families resulted in a more severe phenotype, with significant weight reduction in both heterozygous (16%; $P = 4.05 \times 10^{-4}$) and homozygous (52%; $P = 8.44 \times 10^{-9}$) mice. Finally, the weight of miR-17~92$^{\Delta 17,18,92/+}$ mice was comparable to that of miR-17~92$^{\Delta/+}$ mice (**Fig. 2a**,**b**).

A relative shortening of the fifth mesophalanx (brachymesophalangy) of the forelimb is another characteristic feature of FS2 recapitulated in miR-17~92$^{\Delta/+}$ mice. In miR-17~92$^{\Delta/\Delta}$ mice, forelimb abnormalities were more severe and include absence of the fifth mesophalanx, as well as fusion of the proximal carpal bones[8] (**Fig. 2c**, **Supplementary Fig. 3a** and **Supplementary Table 2**). Among the single-seed mutants, only hemizygous or homozygous deletion of the miR-17 seed family resulted in a significant shortening

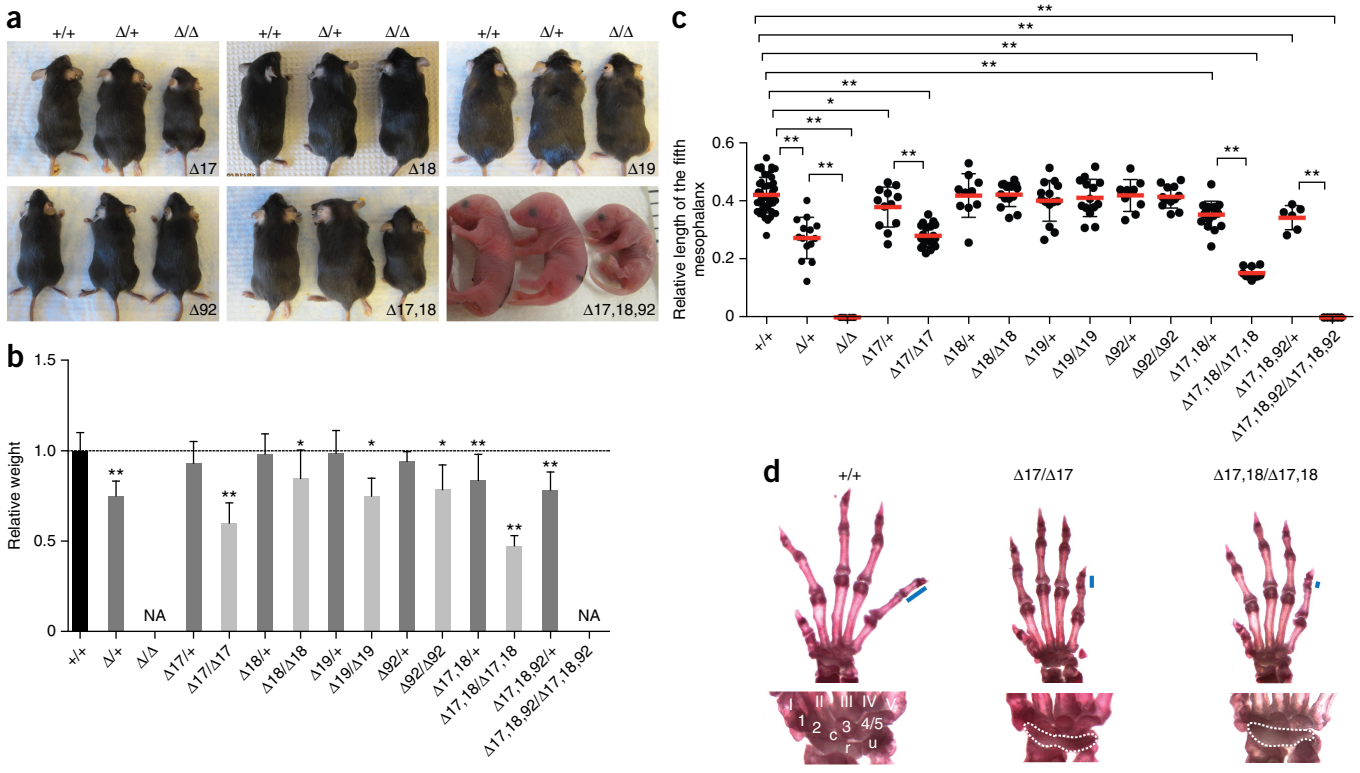

Figure 2 Feingold syndrome (FS2) features in miR-17~92–mutant mice. (**a**) Macroscopic appearance of mice from the miR-17~92 allelic series, including wild-type (+/+), heterozygous (Δ/+) and homozygous-mutant (Δ/Δ) mice. (**b**) Mean weights of 4- to 5-week-old miR-17~92$^{+/+}$ ($n = 77$), miR-17~92$^{\Delta 17\sim 92/+}$ ($n = 13$), miR-17~92$^{\Delta 17/+}$ ($n = 21$), miR-17~92$^{\Delta 17/\Delta 17}$ ($n = 11$), miR-17~92$^{\Delta 18/+}$ ($n = 26$), miR-17~92$^{\Delta 18/\Delta 18}$ ($n = 17$), miR-17~92$^{\Delta 19/+}$ ($n = 19$), miR-17~92$^{\Delta 19/\Delta 19}$ ($n = 6$), miR-17~92$^{\Delta 92/+}$ ($n = 9$), miR-17~92$^{\Delta 92/\Delta 92}$ ($n = 9$), miR-17~92$^{\Delta 17,18/+}$ ($n = 22$), miR-17~92$^{\Delta 17,18/\Delta 17,18}$ ($n = 7$) and miR-17~92$^{\Delta 17,18,92/+}$ ($n = 12$) mice, normalized to sex- and age-matched controls. (**c**) Mean length of the fifth mesophalanx relative to the metacarpal bone. (**d**) Top, representative pictures of forelimb autopods of wild-type, miR-17~92$^{\Delta 17/\Delta 17}$ and miR-17~92$^{\Delta 17,18/\Delta 17,18}$ adult mice. Blue bars represent the length of the mesophalanx. Bottom, detailed view of wrist bones. Digits are numbered I–V. Carpal bones are labeled 1–3 and 4/5, c (central element), u (*ulnare*) and r (*radiale*). Fusion of carpal bones is highlighted with a dashed line. Error bars, s.d. $^*P < 0.05$, $^{**}P < 0.001$, two-tailed *t* test, NA, not available.

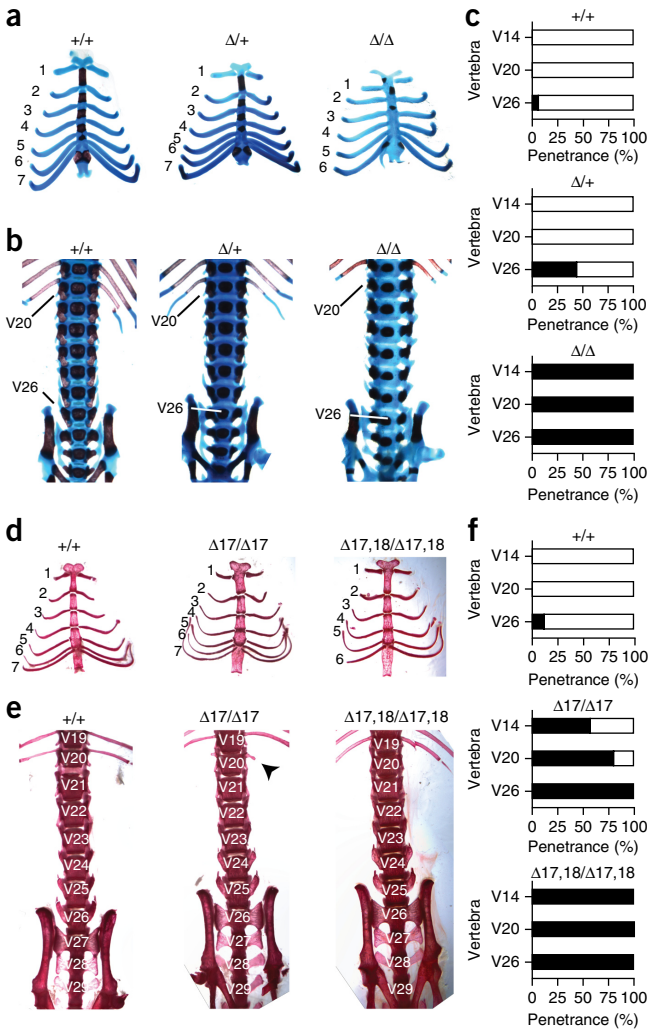

Figure 3 miR-17~92 regulates axial patterning. (**a**) Alcian blue– and Alizarin red–stained rib cages from miR-17~92$^{+/+}$, miR-17~92$^{\Delta/+}$ and miR-17~92$^{\Delta/\Delta}$ embryos at embryonic day (E) 18.5. (**b**) Ventral view of the axial skeleton. The positions of V20 and V26 are indicated. (**c**) Percentage of mice showing vertebral transformations (black) or normal vertebral identity (white) in miR-17~92$^{+/+}$ (n = 20), miR-17~92$^{\Delta/+}$ (n = 28) and miR-17~92$^{\Delta/\Delta}$ (n = 10) mice. (**d**) Alizarin red–stained rib cages from wild-type, miR-17~92$^{\Delta17/\Delta17}$ and miR-17~92$^{\Delta17,18/\Delta17,18}$ adult mice. (**e**) Ventral view of the axial skeleton. The arrowhead indicates a rudimental rib. (**f**) Percentage of mutant mice showing vertebral transformations (black) or normal vertebral identity (white) in miR-17~92$^{+/+}$ (n = 97), miR-17~92$^{\Delta17/\Delta17}$ (n = 9) and miR-17~92$^{\Delta17,18/\Delta17,18}$ (n = 7) mice.

of the fifth mesophalanx (**Fig. 2c**,**d**). A fraction of miR-17~92$^{\Delta17/\Delta17}$ mice, but not mice homozygous for the other single-seed mutant alleles, also displayed fusion of the proximal carpal bones. miR-17~92$^{\Delta17,18/\Delta17,18}$ mutant mice showed more severe phenotypes than mice carrying deletion of the miR-17 family alone, and further deletion of *Mir92-1* (miR-17~92$^{\Delta17,18,92/\Delta17,18,92}$) fully recapitulated the phenotypes seen in miR-17~92 loss-of-function mice (**Fig. 2c** and **Supplementary Fig. 3a**,**b**).

The role of the miR-17~92 cluster in FS2 compelled us to further analyze skeletal development in the absence of the entire cluster or of its individual components (**Supplementary Tables 2**–**4**). Through this analysis, we found that loss of miR-17~92 affected a key event during the formation of the mammalian skeleton: its patterning along the anterior-posterior axis, which leads to the differentiation of morphologically distinct skeletal segments[27,28] (**Supplementary Fig. 3c**). Homeotic transformations in miR-17~92$^{\Delta/\Delta}$ mice were fully penetrant and affected multiple skeletal segments (**Fig. 3a**–**c** and **Supplementary Fig. 3c**,**d**). Specifically, V14—which in wild-type mice is the last vertebra of the rib cage—was transformed into the first vertebra with floating ribs (ribs that do not attach to the sternum; n = 10/10) (**Fig. 3a**). We observed a unilateral (n = 3/10) or bilateral (n = 7/10) loss of ribs on V20 and a transformation of V26 from the last lumbar vertebra into the first sacral vertebra (n = 10/10) (**Fig. 3b**,**c**, **Supplementary Fig. 3d** and **Supplementary Table 3**). We also observed transformations at the lumbar-sacral level in 46% of heterozygous mice, indicating a dose-dependent role of this cluster in axial patterning.

We next examined axial patterning in mice from the allelic series (**Fig. 3d**–**f** and **Supplementary Table 4**). Among the single-seed mutants, only those harboring deletion of the miR-17 seed family displayed transformations similar to those seen in the absence of the full cluster. Simultaneous deletion of the miR-17 and miR-18 families fully recapitulated the phenotypes seen in miR-17~92$^{\Delta/\Delta}$ null mice. These results demonstrate a previously unappreciated role for the miR-17~92 cluster in patterning of the axial skeleton, identify the miR-17 seed family as the main effector of this function and provide a direct link between mutation of a miRNA gene and homeotic transformations.

The miR-17 and miR-18 families regulate B cell development

In miR-17~92–deficient mice, early B cell development was characterized by a partial block at the pro-B to pre-B transition due to increased apoptosis[7]. Among the mice mutant for a single-seed family, only miR-17~92$^{\Delta17/\Delta17}$ mice displayed a statistically significant reduction in pre-B cell numbers (**Fig. 4a**,**b**). This phenotype was exacerbated in miR-17~92$^{\Delta17,18/\Delta17,18}$ mice, once more demonstrating cooperation among these two highly related miRNA families. Consistent with a predominant role for the miR-17 seed family in regulating the pro- to pre-B transition, we observed a significant increase in the fraction of apoptotic pre-B cells in miR-17~92$^{\Delta17/\Delta17}$ and miR-17~92$^{\Delta17,18/\Delta17,18}$ mice in comparison to wild-type mice (**Fig. 4c**), specifically at the pre-BII stage (**Supplementary Fig. 4a**,**b**). These mice also displayed a decrease in the ratio of splenic B cells to T cells and myeloid cells. However, further maturation of B cells in the spleen was unaffected, and spleens appeared histologically normal (**Fig. 4d** and **Supplementary Fig. 4d**,**e**).

On the basis of these results, we conclude that members of the miR-17 and miR-18 seed families have a central role in modulating pre-B cell survival and early B cell development.

Loss of miR-19 impairs Myc-driven tumorigenesis

Ectopic expression studies previously demonstrated that the tumor-promoting activity of miR-17~92 is largely determined by miR-19a and miR-19b-1 (hereafter collectively referred to as miR-19). miR-19 overexpression can recapitulate the ability of miR-17~92 to cooperate with the *Myc* oncogene in driving B cell lymphomagenesis[21]. In addition, lymphoma cells derived from transgenic mice in which ectopic expression of *Myc* is driven by the Eμ enhancer (Eμ-*Myc* mice) display increased apoptosis upon acute deletion of the entire miR-17~92 cluster, a phenotype that can be entirely rescued by reintroduction of miR-19 alone[26]. On the basis of these results and the observation that the miR-17~92 cluster is a direct transcriptional target of Myc[17] (**Fig. 5a**), we hypothesized that upregulation

of endogenous miR-19 by Myc might have a role in tumor initiation and progression, even in the absence of ectopic expression of these miRNAs.

To test this hypothesis, we monitored cohorts of Eμ-*Myc*; miR-17~92$^{+/+}$, Eμ-*Myc*; miR-17~92$^{\Delta 19/+}$ and Eμ-*Myc*; miR-17~92$^{\Delta 19/\Delta 19}$ mice for the appearance of palpable lymphomas and overall survival. Whereas control Eμ-*Myc* mice developed lymphomas with the expected latency, deletion of miR-19 resulted in a dosage-dependent increase in tumor-free and overall survival (**Fig. 5b** and **Supplementary Fig. 5a**). miR-19–deficient mice that eventually succumbed to disease developed tumors markedly biased toward a more mature immunophenotype (**Supplementary Fig. 5b**). Deletion of *Mir18* and *Mir92-1* had minimal or no impact on Eμ-*Myc*–driven lymphomagenesis (**Supplementary Fig. 5d**), whereas targeted deletion of the miR-17 seed family resulted in a significant ($P < 0.001$) delay in tumor latency, presumably as a consequence of the reduced number of pre-B cells (**Supplementary Fig. 5d**). The increased latency and shift in the immunophenotype of lymphomas in Eμ-*Myc*; miR-17~92$^{\Delta 19/\Delta 19}$ mice suggest that the miR-19 seed family has a permissive role in the transformation of early B cell progenitors by Myc.

To determine whether absence of miR-19 impaired the early stages of Myc-driven lymphomagenesis, we examined the bone marrow of young (5-week-old) Eμ-*Myc* mice, which is typically characterized by a preneoplastic accumulation of pre-B cells[29,30] (**Fig. 5c**,**d**). Strikingly, this accumulation was entirely absent in age-matched Eμ-*Myc*; miR-17~92$^{\Delta 19/\Delta 19}$ mice. This was not owing to an inability of the *Myc* oncogene to promote hyperproliferation in the absence of miR-19 (**Supplementary Fig. 5c**,**e**). Rather, the increase in pre-B cell proliferation was counterbalanced by a concomitant marked increase in apoptosis (**Fig. 5e**).

It is worth noting that this role of miR-19 in suppressing apoptosis becomes evident only in the context of oncogenic levels of Myc, whereas loss of miR-19 expression does not impair normal pre-B cell development or survival (**Figs. 4a** and **5e**).

We next sought to determine whether miR-19 has a more general role in Myc-driven tumorigenesis. Up to one-third of human prostate

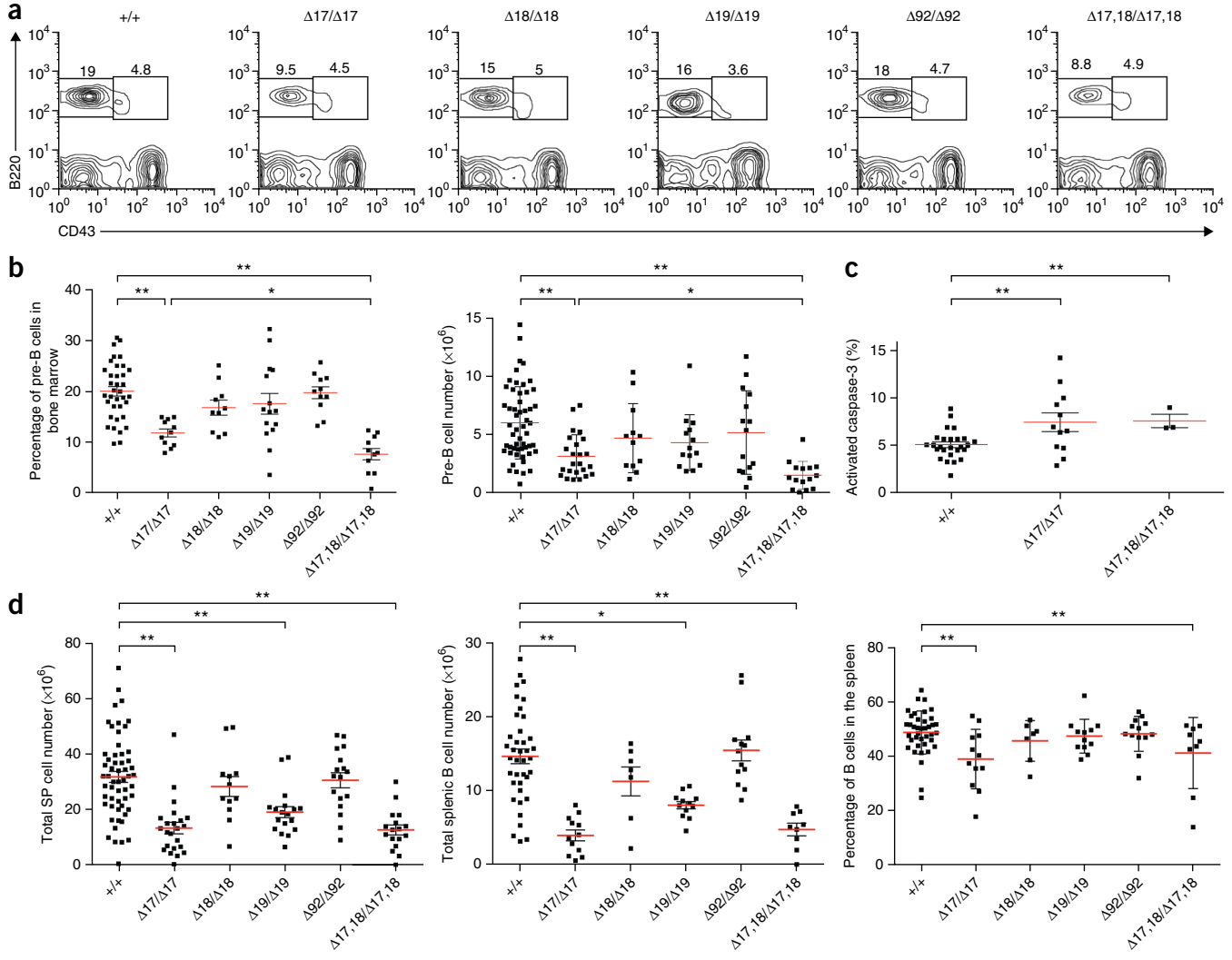

Figure 4 Analysis of B cell development in the miR-17~92 allelic series. (**a**) Flow cytometry plots showing the percentages of bone marrow–derived pro-B cells (IgM$^-$B220$^+$CD43$^+$) and pre-B cells (IgM$^-$B220$^+$CD43$^-$) in 5- to 6-week-old wild-type and homozygous-mutant mice. (**b**) Quantification of the pre-B cell percentage and absolute pre-B cell number ($n > 10$). (**c**) Percentage of pre-B-cells positive for cleaved caspase-3 in 5- to 6-week-old wild-type, miR-17~92$^{\Delta 17/\Delta 17}$ and miR-17~92$^{\Delta 17,18/\Delta 17,18}$ mice ($n > 3$). (**d**) Total number of splenocytes and B cells as well as the percentage of B cells in the spleen. Red bars indicate the average. $^*P < 0.05$, $^{**}P < 0.001$, two-tailed *t* test.

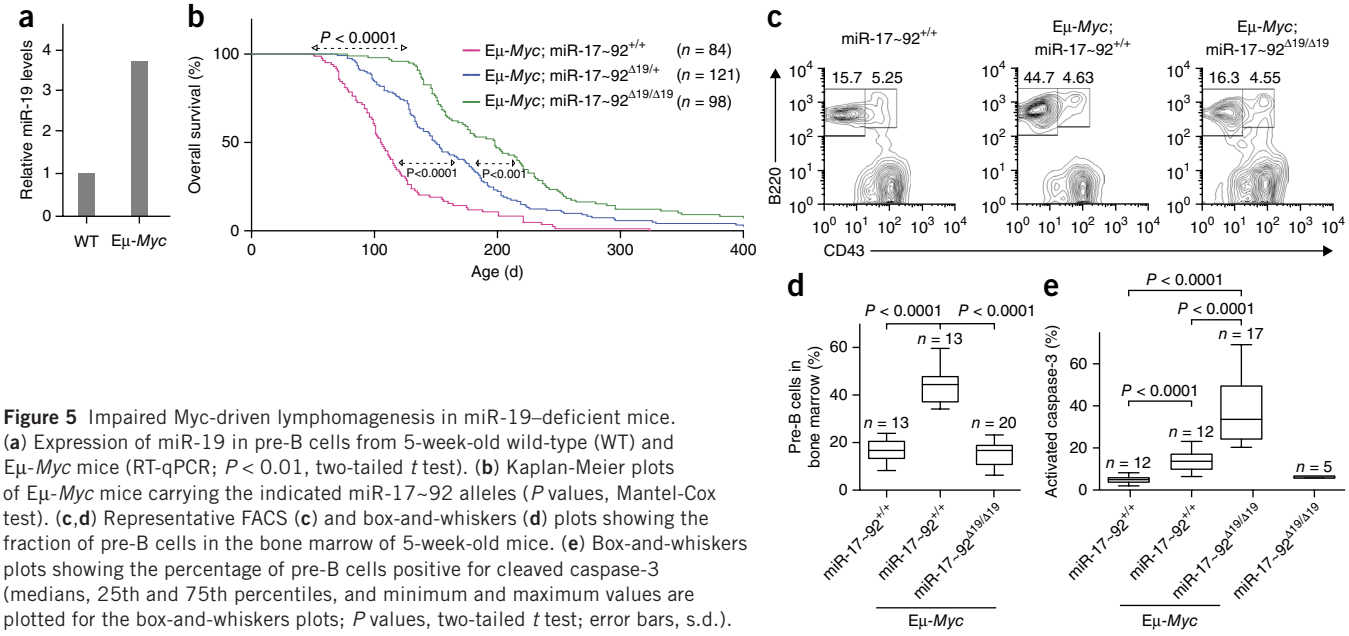

Figure 5 Impaired Myc-driven lymphomagenesis in miR-19–deficient mice. (**a**) Expression of miR-19 in pre-B cells from 5-week-old wild-type (WT) and Eμ-*Myc* mice (RT-qPCR; $P < 0.01$, two-tailed *t* test). (**b**) Kaplan-Meier plots of Eμ-*Myc* mice carrying the indicated miR-17~92 alleles (*P* values, Mantel-Cox test). (**c**,**d**) Representative FACS (**c**) and box-and-whiskers (**d**) plots showing the fraction of pre-B cells in the bone marrow of 5-week-old mice. (**e**) Box-and-whiskers plots showing the percentage of pre-B cells positive for cleaved caspase-3 (medians, 25th and 75th percentiles, and minimum and maximum values are plotted for the box-and-whiskers plots; *P* values, two-tailed *t* test; error bars, s.d.).

cancers harbor genomic amplification of the *MYC* locus[31,32], and mice expressing a *MYC* transgene under the control of the prostate-specific *Pbsn* (probasin) promoter containing two additional androgen-inducible elements (Hi-Myc transgenic mice) develop invasive prostatic adenocarcinomas at 6–12 months of age[33].

To examine the role of miR-19 in this context, we aged cohorts of Hi-Myc; miR-17~92$^{+/+}$ and Hi-Myc; miR-17~92$^{\Delta19/\Delta19}$ mice. At 8 weeks of age, Hi-Myc; miR-17~92$^{+/+}$ male mice displayed extensive signs of prostatic intraepithelial neoplasia (PIN) (**Supplementary Fig. 6a**), as previously described[33]. By contrast, the prostates of age-matched Hi-Myc; miR-17~92$^{\Delta19/\Delta19}$ mice appeared largely normal, with only occasional foci of PIN. Immunohistochemistry for cleaved caspase-3 also showed that, in this context, absence of miR-19 caused a significant ($P < 0.001$) increase in apoptosis in response to the *Myc* oncogene (**Supplementary Fig. 6b**,**c**).

Even more dramatic were the consequences on tumor progression. In Hi-Myc control mice, we detected invasive adenocarcinomas by 8 months of age, and these were present in all mice by 10 months (**Supplementary Fig. 6d**,**e**). In contrast, miR-19–deficient mice showed a largely unaffected prostate even at 12 months of age; by 14 months, only one-third of mice lacking miR-19 displayed histological evidence of invasive cancer. Delayed tumor progression was confirmed by non-invasive imaging studies (**Supplementary Fig. 6f**,**g**).

By demonstrating a critical function in two distinct Myc-driven cancer models, our results establish miR-19 as a central component of the Myc oncogenic network.

Genome-wide analysis of miR-17~92 targets *in vivo*

To gain insights into the physiological targets of miR-17~92, we next sought to explore how targeted deletion of individual components affects gene expression *in vivo*. Although miRNA-mediated regulation ultimately controls protein output, previous studies comparing proteomic and RNA expression profiling have demonstrated that most if not all of the changes in protein levels can be explained by changes in mRNA levels[34–36].

We performed RNA-seq experiments on RNA from hearts and tail buds microdissected from the various miR-17~92–mutant embryos. These tissues were chosen because loss of miR-17~92 in these tissues resulted in some of the most prominent developmental defects described here (**Figs. 1–3**). We used only embryos at the 20- to 22-somite stage, to minimize variability and because this stage immediately precedes the appearance of the first detectable developmental abnormalities in miR-17~92–null mice.

Cumulative distribution fraction (CDF) plots of $\log_2$ (fold change in expression) showed that, in each mutant strain, the predicted targets of the deleted miRNA(s) were preferentially upregulated in comparison to their levels in wild-type embryos (**Supplementary Fig. 7** and **Supplementary Table 5**), demonstrating that our analysis captures changes in gene expression caused by targeted deletion of the miR-17~92 cluster and its various components.

To examine the relative contribution of each seed family and the functional interactions of the families in the modulation of targets, we next visualized the genes significantly (false discovery rate (FDR) ≤ 0.1)

Figure 6 Genome-wide identification of genes regulated by members of the miR-17~92 cluster. (**a**) Circos plot of differentially expressed genes (FDR ≤ 0.1) in the tail bud of miR-17~92–mutant embryos. Each sector of the plot corresponds to a different miR-17~92 mutant allele. To reduce complexity, only the complete knockout (Δ/Δ) and the four single-seed mutant alleles are shown (for additional Circos plots—including ones generated from the heart data set—see **Supplementary Figs. 8–11**). Genes with predicted binding sites for one or more of the deleted miRNAs are grouped under the darker portion of each sector. A scatter plot of $\log_2$ (fold-change expression) is presented in the intermediate circle, with up- and downregulated genes labeled in red and blue, respectively. Presence of predicted binding sites for the various components of the miR-17~92 cluster is indicated by a colored bar in the inner circle. Genes differentially expressed in more than one genotype are joined by links. Links are colored if the gene has predicted binding sites for miR-17~92 component(s); otherwise, they are shown in light gray. (**b**) Bar plot of GO terms enriched among the most significant differentially expressed genes (FDR ≤ 0.01 and $\log_2$ (fold change) ≥ 0.26) in miR-17~92$^{\Delta/\Delta}$ tail bud (top) or heart (bottom). Only terms relevant to cardiac or skeletal development are shown. The red dashed vertical line marks a nominal enrichment *P* value of 0.05. (**c**) Genes contributing to the enriched GO terms shown in **b**. Diamonds indicate predicted miR-17~92 targets; circles indicate presumed indirect targets. Color reflects $\log_2$ (fold change) for expression.

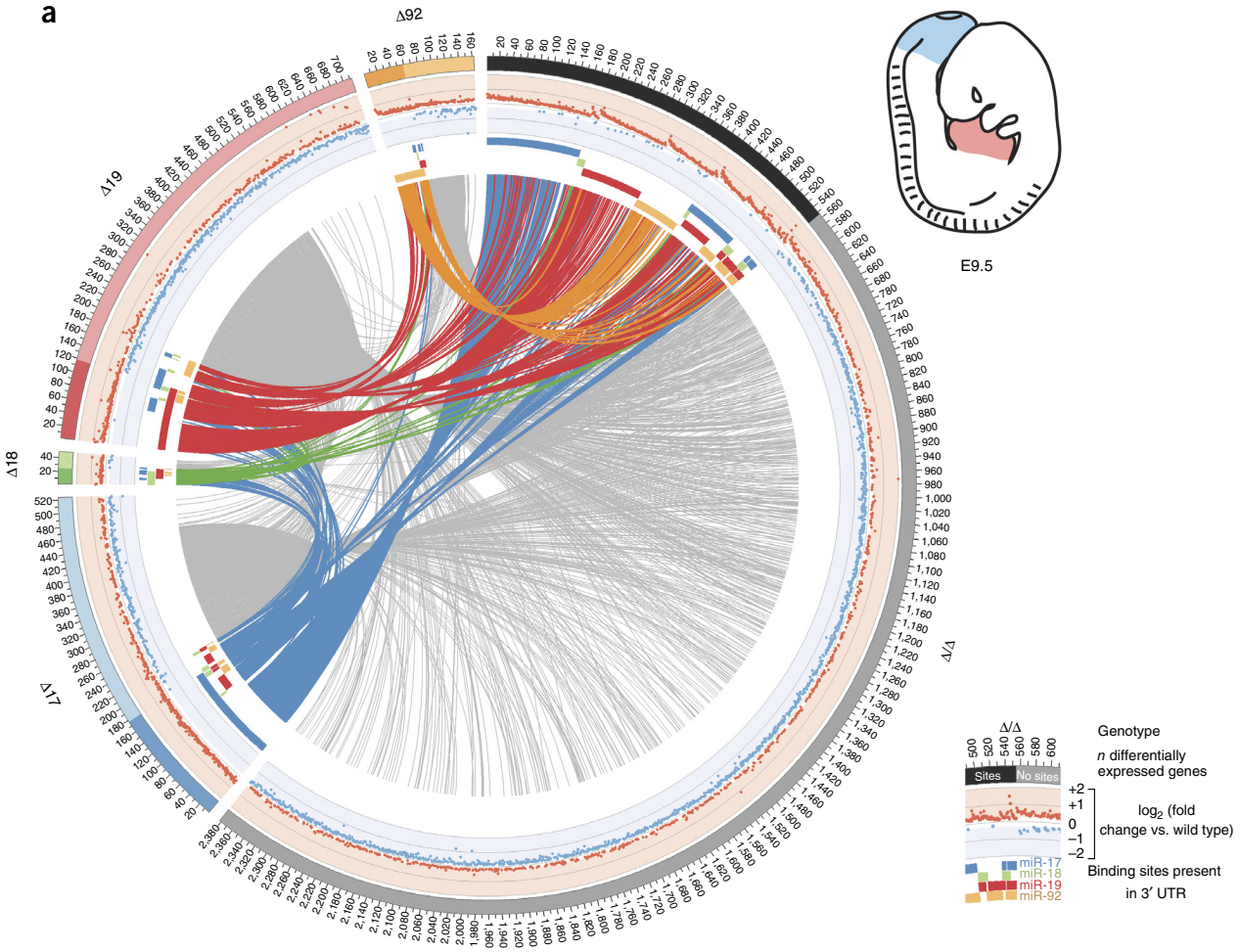

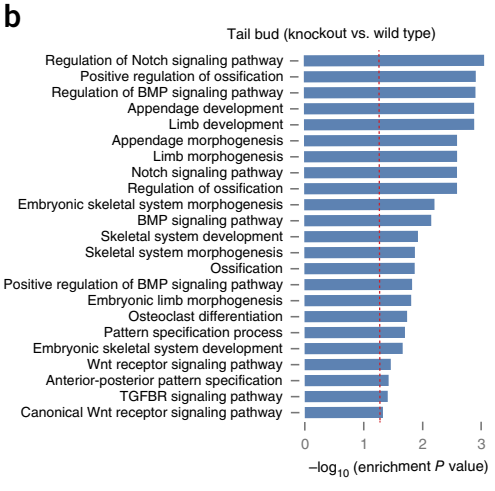

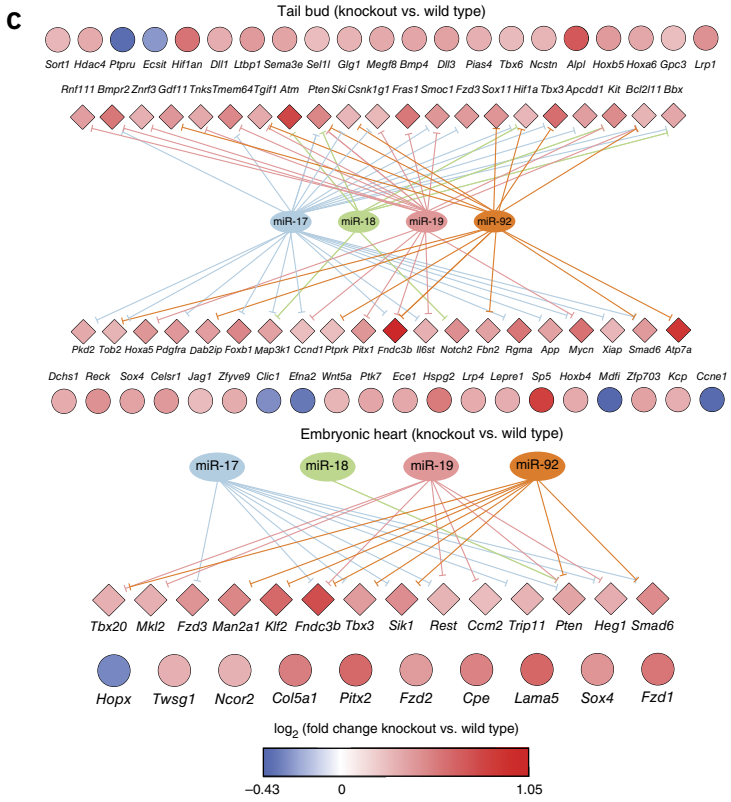

deregulated in each genotype using the Circos package[37] (**Fig. 6a** and **Supplementary Figs. 8–11**). In these plots, genes deregulated in two or more mutant mice are joined by links. For each gene, the plots also provide information regarding the direction and amplitude of deregulation (in the middle track) and the presence of predicted binding sites for the various components of the miR-17~92 cluster (in the inner track) (see **Fig. 6a** for additional details).

These plots provide a high-level view of the regulatory activity of miR-17~92 *in vivo* and illustrate, at the molecular level, the complex interactions existing among the various components of the cluster. Several conclusions can be drawn from their analysis. First, it is immediately evident that the four seed families encoded by miR-17~92 differ greatly in the number of genes they regulate *in vivo*. For example, only a handful of genes are affected by loss of miR-18, whereas the miR-17 and miR-19 seed families modulate the expression of the largest number of genes. It is also worth noting that the extent of gene regulation by the cluster is dependent on context: nearly four times as many genes are affected by loss of miR-17~92 in the tail bud as are in the embryonic heart.

Another conclusion stems from the observation that the number of genes whose expression is deregulated upon deletion of the entire miR-17~92 cluster is substantially greater than the sum of the genes deregulated in the single-seed mutants (**Fig. 6a**). This finding supports the idea that the various members of the miR-17~92 cluster cooperatively regulate, either directly or indirectly, a large number of genes. Interestingly, the number of genes differentially expressed in the miR-17~92$^{\Delta 17,18}$ double-seed mutant was much greater than the sum of the genes deregulated in the miR-17~92$^{\Delta 17}$ and miR-17~92$^{\Delta 18}$ single-seed mutants (**Supplementary Figs. 8–11**), indicating strong cooperation between these two closely related miRNA families.

The last and perhaps most notable conclusion is that, although loss of miR-17~92 or its individual components results in reproducible deregulation of hundreds of genes, the amplitude of this effect is invariably very modest, with the vast majority of genes changing in expression by less than one $\log_2$ (fold change) compared to wild-type embryos (**Fig. 6**, **Supplementary Figs. 8–11** and **Supplementary Table 5**). Interestingly, this is not only true for differentially expressed genes that have predicted binding sites for miR-17~92 components in their 3′ UTRs—the 'direct' targets—but is also true for genes that are regulated indirectly by miR-17~92 miRNAs. This observation indicates that the modest effects on direct targets are not amplified downstream and has important implications because it suggests that, rather than acting as genetic switches for specific signaling pathways or transcription factors, the miRNAs in the miR-17~92 cluster act as fine-tuners, ensuring that the expression of a large number of genes stays within a very narrow range at critical developmental stages. As a consequence, it is unlikely that the complexity of phenotypes observed in the various mutant mice described here can be assigned to loss of repression of one or a few key targets.

To gain further insights into the genes regulated by miR-17~92, we searched for enrichment of Gene Ontology (GO) terms within the subset of genes deregulated in miR-17~92$^{\Delta/\Delta}$ embryos (**Fig. 6b** and **Supplementary Table 6**). Consistent with the phenotypes observed in miR-17~92–null mice, in the heart data set, we found significant enrichment of GO terms associated with cardiac development and, in particular, the development of the ventricular septum. Similarly, GO terms related to ossification, skeletal development and patterning were significantly over-represented in the tail bud data set. The differentially expressed genes contributing to these terms, their fold change in expression in comparison to wild-type embryos and their predicted interactions with members of the miR-17~92 cluster are shown in **Figure 6c**.

Many of the genes contributing to the GO terms in the heart, such as *Tbx3*, *Tbx20*, *Smad6*, *Heg1*, *Klf2* and *Trip11*, are direct targets of the cluster for which there is experimental evidence that perturbation of their expression is sufficient to induce cardiac defects in vertebrates[38–44]. Analogously, GO terms from the tail bud data set included direct and indirect targets of miR-17~92 component miRNAs involved in mesoderm formation (*Bmp4* and *Bmpr2*)[45,46], specification (*Tbx6*)[47], segmentation (*Notch2*, *Jag1*, *Dll3* and *Dll1*)[48,49], axial patterning (*Gdf11*, *Hoxa5*, *Hoxa6* and *Hoxb4*)[50,51] and limb development (*Tbx3* and *Bmp4*)[52,53].

GO assignments are imperfect and limited by current knowledge of embryonic development; hence, it is likely that this analysis underestimates the number of genes whose deregulation in miR-17~92–deficient mice contributes to the developmental defects observed. Nevertheless, the picture emerging from our work is consistent with a model in which members of the miR-17~92 cluster have evolved to coordinately fine-tune the expression of a wide network of genes involved in multiple aspects of mammalian development. We propose that it is the concomitant loss of fine-tuning of these genes, rather than the deregulation of a single or a few key targets, that causes the complex phenotypes observed in miR-17~92–mutant mice.

DISCUSSION

The allelic series of miR-17~92–mutant mice and the associated RNA-seq data set reported here offer an unprecedented view of the functional organization of a multifamily miRNA cluster. There are at least five aspects of this work that we believe are of general relevance.

First, we provide direct genetic evidence that strong functional specialization and cooperation can coexist among members of the same polycistronic cluster. A clear example of functional specialization is represented by the unique role of the miR-17 seed family in modulating axial patterning. By contrast, perinatal lethality, cardiac defects and lung hypoplasia are clear examples of functional cooperation. We also identify cases in which one seed family has a dominant but not unique role, as exemplified by the role of the miR-17 seed family in pre-B cell survival and in digit development.

Second, we uncover an unexpected role for the miR-17~92 cluster in modulating skeletal patterning, as shown by the occurrence of fully penetrant homeotic transformations in miR-17~92$^{\Delta/\Delta}$ and miR-17~92$^{\Delta 17/\Delta 17}$ mice. Despite multiple reports linking miRNAs to embryonic patterning[54–56], loss-of-function mutations of a miRNA gene have not previously been linked to disrupted patterning of embryonic axes in mice. This discovery also lends support to the idea[57] that expansion of the miR-17 seed family was temporally and functionally connected to the origin of vertebrates and with the concomitant genome-wide duplications that resulted in the formation of the four Hox gene clusters.

Third, we define members of the miR-19 seed family as key components of the oncogenic network orchestrated by Myc. The observation that miR-19–deficient mice are remarkably resistant to Myc-driven tumorigenesis in two distinct tumor models demonstrates that this miRNA family is a critical downstream effector of Myc and has a crucial role in Myc-driven tumor initiation and progression. In this context, a surprising finding is that, in the absence of oncogenic levels of Myc, loss of miR-19 expression has no obvious detrimental effects on pre-B cell differentiation or on prostate homeostasis. This observation has obvious therapeutic implications because it suggests that pharmacologic inhibition of miR-19 in patients affected by tumors expressing oncogenic levels of MYC could have anticancer effects

with little toxicity. It is tempting to speculate that miR-19 induction by Myc might be part of the physiological response to conditions requiring the rapid and transient expansion of specific cell populations in response to acute stresses.

Fourth, the RNA-seq data derived from this allelic series of mutant mice provide a unique and to some extent surprising view of the physiological targets of a polycistronic miRNA cluster *in vivo*. We have already discussed some of the specific implications with respect to miR-17~92 functions. Here we would like to emphasize that our findings strongly support the notion that, in animals, many miRNAs have evolved not to act as genetic switches of specific pathways or individual targets but rather to modulate expression of large gene networks. If our interpretation is correct, the search for individual 'key targets' that can explain the biological properties of a given miRNA might prove futile if not misleading.

Finally, the six new miR-17~92–mutant strains reported here represent a valuable resource for the noncoding RNA field, as they will accelerate and facilitate further mechanistic investigations into the complex developmental and oncogenic functions of this cluster. Likewise, the RNA-seq data sets we have generated will provide the scientific community with unprecedented opportunities to explore the molecular determinants of miRNA targeting in a physiological, *in vivo* setting.

URLs. TargetScan, http://www.targetscan.org/.

METHODS

Methods and any associated references are available in the online version of the paper.

Accession codes. The small-RNA sequencing data are available from the Gene Expression Omnibus (GEO) under accession GSE63660. The embryonic RNA-seq data are available from GEO under accession GSE63813.

Note: Any Supplementary Information and Source Data files are available in the online version of the paper.

ACKNOWLEDGMENTS

We thank J. Hollenstein for editing the manuscript and members of the Ventura laboratory for helpful discussions. The authors greatly acknowledge the contribution of the Weill Cornell Epigenomics Core. This work was funded by grants from the US National Institutes of Health/National Cancer Institute (R01CA149707 to A.V. and Core grant P30CA008748), the STARR Consortium (to A.V. and D.B.), the Geoffrey Beene Cancer Foundation (to A.V.), the Gabrielle's Angel Foundation (to A.V.), the Leukemia Lymphoma Society (to Y.-C.H.), the American Italian Cancer Foundation (to C.B.) and a US National Institutes of Health training grant (F31CA168356 to C.P.C.).

AUTHOR CONTRIBUTIONS

A.V., J.A.V., Y.-C.H. and P.M. conceived the project and designed the experiments. A.V., J.A.V. and Y.-C.H. wrote the manuscript. A.V., E.Y., P.O. and P.M. generated the mouse strains. Y.-C.H. characterized overall viability. Y.-C.H. and P.M. characterized the hematopoietic phenotypes. J.A.V., E.Y. and L.S. characterized the skeletal phenotypes. P.M., B.C. and C.B. characterized the oncogenic phenotypes. Y.-C.H., J.A.V. and C.P.C. generated the small-RNA libraries. Y.-C.H. and J.A.V. generated the RNA-seq libraries. A.V., D.B., C.L., I.S. and A.J.G. performed the computational analysis for the RNA-seq data. D.B. and C.L. contributed equally to the computational analysis.

COMPETING FINANCIAL INTERESTS

The authors declare no competing financial interests.

1. Bartel, D.P. MicroRNAs: target recognition and regulatory functions. *Cell* **136**, 215–233 (2009).
2. Lai, E.C. Micro RNAs are complementary to 3′ UTR sequence motifs that mediate negative post-transcriptional regulation. *Nat. Genet.* **30**, 363–364 (2002).
3. Lewis, B.P., Burge, C.B. & Bartel, D.P. Conserved seed pairing, often flanked by adenosines, indicates that thousands of human genes are microRNA targets. *Cell* **120**, 15–20 (2005).
4. Lim, L.P. *et al.* Microarray analysis shows that some microRNAs downregulate large numbers of target mRNAs. *Nature* **433**, 769–773 (2005).
5. Chiang, H.R. *et al.* Mammalian microRNAs: experimental evaluation of novel and previously annotated genes. *Genes Dev.* **24**, 992–1009 (2010).
6. Concepcion, C.P., Bonetti, C. & Ventura, A. The microRNA-17-92 family of microRNA clusters in development and disease. *Cancer J.* **18**, 262–267 (2012).
7. Ventura, A. *et al.* Targeted deletion reveals essential and overlapping functions of the miR-17~92 family of miRNA clusters. *Cell* **132**, 875–886 (2008).
8. de Pontual, L. *et al.* Germline deletion of the miR-17~92 cluster causes skeletal and growth defects in humans. *Nat. Genet.* **43**, 1026–1030 (2011).
9. Feingold, M., Hall, B.D., Lacassie, Y. & Martinez-Frias, M.L. Syndrome of microcephaly, facial and hand abnormalities, tracheoesophageal fistula, duodenal atresia, and developmental delay. *Am. J. Med. Genet.* **69**, 245–249 (1997).
10. Ota, A. *et al.* Identification and characterization of a novel gene, *C13orf25*, as a target for 13q31-q32 amplification in malignant lymphoma. *Cancer Res.* **64**, 3087–3095 (2004).
11. Hayashita, Y. *et al.* A polycistronic microRNA cluster, miR-17-92, is overexpressed in human lung cancers and enhances cell proliferation. *Cancer Res.* **65**, 9628–9632 (2005).
12. He, L. *et al.* A microRNA polycistron as a potential human oncogene. *Nature* **435**, 828–833 (2005).
13. Kumps, C. *et al.* Focal DNA copy number changes in neuroblastoma target MYCN regulated genes. *PLoS ONE* **8**, e52321 (2013).
14. Mi, S. *et al.* Aberrant overexpression and function of the miR-17-92 cluster in *MLL*-rearranged acute leukemia. *Proc. Natl. Acad. Sci. USA* **107**, 3710–3715 (2010).
15. Schetter, A.J. *et al.* MicroRNA expression profiles associated with prognosis and therapeutic outcome in colon adenocarcinoma. *J. Am. Med. Assoc.* **299**, 425–436 (2008).
16. Thayanithy, V. *et al.* Perturbation of 14q32 miRNAs-cMYC gene network in osteosarcoma. *Bone* **50**, 171–181 (2012).
17. O'Donnell, K.A., Wentzel, E.A., Zeller, K.I., Dang, C.V. & Mendell, J.T. c-Myc–regulated microRNAs modulate E2F1 expression. *Nature* **435**, 839–843 (2005).
18. Conkrite, K. *et al.* miR-17~92 cooperates with RB pathway mutations to promote retinoblastoma. *Genes Dev.* **25**, 1734–1745 (2011).
19. Dews, M. *et al.* Augmentation of tumor angiogenesis by a Myc-activated microRNA cluster. *Nat. Genet.* **38**, 1060–1065 (2006).
20. Jin, H.Y. *et al.* MicroRNA-17~92 plays a causative role in lymphomagenesis by coordinating multiple oncogenic pathways. *EMBO J.* **32**, 2377–2391 (2013).
21. Olive, V. *et al.* miR-19 is a key oncogenic component of mir-17-92. *Genes Dev.* **23**, 2839–2849 (2009).
22. Olive, V. *et al.* A component of the mir-17-92 polycistronic oncomir promotes oncogene-dependent apoptosis. *eLife* **2**, e00822 (2013).
23. Sandhu, S.K. *et al.* B-cell malignancies in microRNA Eμ-miR-17~92 transgenic mice. *Proc. Natl. Acad. Sci. USA* **110**, 18208–18213 (2013).
24. Uziel, T. *et al.* The miR-17~92 cluster collaborates with the Sonic Hedgehog pathway in medulloblastoma. *Proc. Natl. Acad. Sci. USA* **106**, 2812–2817 (2009).
25. Mavrakis, K.J. *et al.* Genome-wide RNA-mediated interference screen identifies miR-19 targets in Notch-induced T-cell acute lymphoblastic leukaemia. *Nat. Cell Biol.* **12**, 372–379 (2010).
26. Mu, P. *et al.* Genetic dissection of the miR-17~92 cluster of microRNAs in Myc-induced B-cell lymphomas. *Genes Dev.* **23**, 2806–2811 (2009).
27. Saga, Y. & Takeda, H. The making of the somite: molecular events in vertebrate segmentation. *Nat. Rev. Genet.* **2**, 835–845 (2001).
28. Wellik, D.M. Hox patterning of the vertebrate axial skeleton. *Dev. Dyn.* **236**, 2454–2463 (2007).
29. Adams, J.M. *et al.* The c-*myc* oncogene driven by immunoglobulin enhancers induces lymphoid malignancy in transgenic mice. *Nature* **318**, 533–538 (1985).
30. Langdon, W.Y., Harris, A.W., Cory, S. & Adams, J.M. The c-*myc* oncogene perturbs B lymphocyte development in Eμ-*myc* transgenic mice. *Cell* **47**, 11–18 (1986).
31. Jenkins, R.B., Qian, J., Lieber, M.M. & Bostwick, D.G. Detection of c-*myc* oncogene amplification and chromosomal anomalies in metastatic prostatic carcinoma by fluorescence *in situ* hybridization. *Cancer Res.* **57**, 524–531 (1997).
32. Qian, J., Jenkins, R.B. & Bostwick, D.G. Detection of chromosomal anomalies and c-*myc* gene amplification in the cribriform pattern of prostatic intraepithelial neoplasia and carcinoma by fluorescence *in situ* hybridization. *Mod. Pathol.* **10**, 1113–1119 (1997).
33. Ellwood-Yen, K. *et al.* Myc-driven murine prostate cancer shares molecular features with human prostate tumors. *Cancer Cell* **4**, 223–238 (2003).
34. Baek, D. *et al.* The impact of microRNAs on protein output. *Nature* **455**, 64–71 (2008).
35. Selbach, M. *et al.* Widespread changes in protein synthesis induced by microRNAs. *Nature* **455**, 58–63 (2008).
36. Eichhorn, S.W. *et al.* mRNA destabilization is the dominant effect of mammalian microRNAs by the time substantial repression ensues. *Mol. Cell* **56**, 104–115 (2014).

37. Krzywinski, M. *et al.* Circos: an information aesthetic for comparative genomics. *Genome Res.* **19**, 1639–1645 (2009).
38. Galvin, K.M. *et al.* A role for Smad6 in development and homeostasis of the cardiovascular system. *Nat. Genet.* **24**, 171–174 (2000).
39. Meneghini, V., Odent, S., Platonova, N., Egeo, A. & Merlo, G.R. Novel *TBX3* mutation data in families with ulnar-mammary syndrome indicate a genotype-phenotype relationship: mutations that do not disrupt the T-domain are associated with less severe limb defects. *Eur. J. Med. Genet.* **49**, 151–158 (2006).
40. Stennard, F.A. *et al.* Murine T-box transcription factor Tbx20 acts as a repressor during heart development, and is essential for adult heart integrity, function and adaptation. *Development* **132**, 2451–2462 (2005).
41. Kirk, E.P. *et al.* Mutations in cardiac T-box factor gene *TBX20* are associated with diverse cardiac pathologies, including defects of septation and valvulogenesis and cardiomyopathy. *Am. J. Hum. Genet.* **81**, 280–291 (2007).
42. Kleaveland, B. *et al.* Regulation of cardiovascular development and integrity by the heart of glass–cerebral cavernous malformation protein pathway. *Nat. Med.* **15**, 169–176 (2009).
43. Lee, J.S. *et al.* Klf2 is an essential regulator of vascular hemodynamic forces *in vivo*. *Dev. Cell* **11**, 845–857 (2006).
44. Follit, J.A. *et al.* The Golgin GMAP210/TRIP11 anchors IFT20 to the Golgi complex. *PLoS Genet.* **4**, e1000315 (2008).
45. Beppu, H. *et al.* BMP type II receptor is required for gastrulation and early development of mouse embryos. *Dev. Biol.* **221**, 249–258 (2000).
46. Winnier, G., Blessing, M., Labosky, P.A. & Hogan, B.L. Bone morphogenetic protein-4 is required for mesoderm formation and patterning in the mouse. *Genes Dev.* **9**, 2105–2116 (1995).
47. Chapman, D.L. & Papaioannou, V.E. Three neural tubes in mouse embryos with mutations in the T-box gene *Tbx6*. *Nature* **391**, 695–697 (1998).
48. Jiang, Y.J. *et al.* Notch signalling and the synchronization of the somite segmentation clock. *Nature* **408**, 475–479 (2000).
49. Pourquié, O. The segmentation clock: converting embryonic time into spatial pattern. *Science* **301**, 328–330 (2003).
50. Deschamps, J. & van Nes, J. Developmental regulation of the Hox genes during axial morphogenesis in the mouse. *Development* **132**, 2931–2942 (2005).
51. McPherron, A.C., Lawler, A.M. & Lee, S.J. Regulation of anterior/posterior patterning of the axial skeleton by growth/differentiation factor 11. *Nat. Genet.* **22**, 260–264 (1999).
52. Selever, J., Liu, W., Lu, M.F., Behringer, R.R. & Martin, J.F. Bmp4 in limb bud mesoderm regulates digit pattern by controlling AER development. *Dev. Biol.* **276**, 268–279 (2004).
53. Davenport, T.G., Jerome-Majewska, L.A. & Papaioannou, V.E. Mammary gland, limb and yolk sac defects in mice lacking *Tbx3*, the gene mutated in human ulnar mammary syndrome. *Development* **130**, 2263–2273 (2003).
54. Yekta, S., Tabin, C.J. & Bartel, D.P. MicroRNAs in the Hox network: an apparent link to posterior prevalence. *Nat. Rev. Genet.* **9**, 789–796 (2008).
55. Hornstein, E. *et al.* The microRNA miR-196 acts upstream of Hoxb8 and Shh in limb development. *Nature* **438**, 671–674 (2005).
56. Ronshaugen, M., Biemar, F., Piel, J., Levine, M. & Lai, E.C. The *Drosophila* microRNA iab-4 causes a dominant homeotic transformation of halteres to wings. *Genes Dev.* **19**, 2947–2952 (2005).
57. Tanzer, A. & Stadler, P.F. Molecular evolution of a microRNA cluster. *J. Mol. Biol.* **339**, 327–335 (2004).

ONLINE METHODS

Mouse husbandry and generation of miR-17~92–mutant mice. miR-17~92$^{\Delta}$, Eμ-*Myc* and Hi-Myc mice have been described previously[7,29,33]. Targeting constructs for the miR-17~92–mutant alleles were generated by modifying the original miR-17~92 conditional targeting construct. Briefly, a 2.2-kb fragment containing one *loxP* site and the sequence for the six pre-miRNAs was retrieved through PmlI-XhoI digestion and cloned into the multiple-cloning site of pBS KS(+). Pre-miRNA sequences were deleted through PCR-mediated mutagenesis, after which the mutated PmlI-XhoI fragment was recloned into the targeting vector. V6.5 ES cells (obtained from R. Jaenisch (Whitehead Institute and Massachusetts Institute of Technology) and tested negative for mycoplasma contamination) were electroporated with the various linearized targeting constructs and selected in standard ES medium containing G418 (Sigma) for 10 d. Recombinant clones were identified by Southern blot using probes that hybridize outside the 5′ and 3′ homology regions as previously described[7]. Two clones for each allele were injected into C57BL/6 blastocysts to generate chimeric mice. To delete the *neo* cassette, mice heterozygous for each allele were crossed to β-actin–Flpe mice[58]. miR-17~92$^{\Delta}$ mice were genotyped as previously described[7]. Mice carrying the remaining miR-17~92 mutant alleles were genotyped using three-primer PCR (p1, 5′-CCTCAAGGGAAAGATGGCAAAC-3′, final concentration of 0.4 μM; p2: 5′-ATAGCCTGAAACCAACTGTGC-3′, final concentration of 0.2 μM; p3: 5′-TAAAGCGCATGCTCCAGAC-3′, final concentration of 0.2 μM), which amplifies a 155-bp band from a wild-type allele (p1-p2), a 237-bp band from all targeted alleles (p1-p3) and a 368-bp band following deletion of the *neo* cassette (p1-p2). Mice were maintained on both mixed 129SvJae × C57BL/6J (B6-129) and pure C57BL/6J backgrounds. All data related to skeletal defects were collected in mice backcrossed to C57BL/6 mice for at least seven generations. Remaining data were collected in mice from B6-129 colonies. No specific randomization procedure was required. For the lymphoma and prostate cancer experiments, the technician monitoring mouse health status was blinded to genotype. All studies and procedures were approved by the Memorial Sloan Kettering Cancer Center Institutional Animal Care and Use Committee. No power analysis was used to predetermine sample size.

Skeletal preparations. E18.5 fetuses were eviscerated, soaked in water for 2–4 h and placed in a 65 °C water bath for 1 min before skinning. Adult mice were euthanized by CO_2 asphyxiation. Eviscerated and skinned mice were fixed in 100% ethanol, stained for cartilage with Alcian blue (150 mg/l Alcian blue 8GX in 80% ethanol and 20% acetic acid) and then stained for bone with Alizarin red (50 mg/l Alizarin red S in 2% potassium hydroxide). Skeletons were stored in clearing solution (40% glycerol, 20% benzyl alcohol and 30% ethanol). Images were captured with a Zeiss Stereo Discovery V8 microscope and processed in Photoshop. Measurements were performed in ImageJ on digitalized images. The investigator scoring skeletal defects was blinded to genotype.

MiRNA detection by quantitative PCR. Total RNA from cells or homogenized tissues was extracted using TRIzol (Invitrogen) following the manufacturer's instructions. Expression of miRNAs was determined with TaqMan miRNA expression assays (Applied Biosystems) according to the manufacturer's instructions. Assays were performed on a minimum of three biological replicates, and results were normalized to sno135 levels.

Flow cytometry analysis. Single-cell suspensions prepared from bone marrow, spleen and tumor samples were stained in FACS buffer (0.5% FBS and 2 mM EDTA in PBS) for B cell, T cell and myeloid cell markers using the following antibodies: B220 (25-0452-81, 552094 and 553092), IgD (553439 and 12-5993-82), CD8 (45-0081-82, 25-0081-82 and 553035), CD11b (553310, 557397 and 17-0112-81), CD25 (clone PC61), CD43 (553270, 12-0431-81 and 560663), CD44 (559250), CD117 (clone 2B8), BP-1 (clone BP-1 (RUO)) and CD24/HSA (clone M1/69 (RUO)) (BD Pharmingen); IgM (12-5790-82, 25-5790-82 and 552867), TCR-β (553170, 12-5961-82, 17-5961-82 and 25-5961-82) and CD4 (48-0042-82 and clones RM4-5 and GK1.5) (eBioscience). Flow cytometry was performed on a FACSCalibur or LSRII (BD Biosciences) flow cytometer. FACS data were analyzed with FlowJo (TreeStar). Apoptosis was measured using the Caspase Detection kit (Red-VAD-FMK or FITC-VAD-FMK, Calbiochem). Cell cycle analysis of pre-B cells was performed using Click-iT EdU Cell Proliferation Assays (Life Technologies) and the FITC BrdU Flow kit (BD Pharmingen).

Histology. Eosin/hematoxylin and immunohistochemistry staining was performed on 5-μm sections of formalin-fixed, paraffin-embedded tissues according to standard protocols. Cleaved caspase-3 was detected with an antibody against Asp175 (9661, Cell Signaling Technology) diluted 1:200 in PBS with 2% BSA. Images were acquired using a Zeiss Apotome microscope equipped with a Zeiss AxioCam MRM camera.

Magnetic resonance imaging. Mouse prostate magnetic resonance images were acquired on a Bruker 4.7T Biospec scanner by the Animal Imaging Core Facility at Memorial Sloan Kettering Cancer Center. A total of 35 images were acquired every 0.9 mm per mouse and used for volumetric calculations.

Small-RNA sequencing. Small-RNA libraries were prepared with a previously published protocol[59] and sequenced as 50-bp single reads on a single HiSeq 2500 lane that generated more than 180 million reads. The sequencing adaptor (5′-TCGTATGCCGTCTTCTGCTTG-3′) was trimmed from the 3′ end of the reads using the FLEXBar tool, and libraries were demuxed using a custom Python script. Reads were mapped to the reference mouse genome (mm9) using STAR aligner[60] with parameter --outFilterMismatchNmax 1 to minimize mismatches to the genome. The resulting sam files were converted to bam format and indexed using SAMtools[61]. MiRNA read counts were computed with featureCounts[62] using miRNA mm9 coordinates downloaded from mirBase (version 18). Reads mapping to multiple sites were counted according to the number of locations to which they mapped, and reads mapping to more than one mature miRNA were counted equally. Finally, miRNA read counts were normalized by geometric mean implemented in the DESeq R package.

RNA sequencing experiment and computational analysis. Total RNA was extracted from microdissected tail buds and embryonic hearts (at the 20- to 22-somite stage; E9.5) of 3 embryos per genotype (48 samples in total). Libraries were prepared using the TruSeq SBS kit v3 according to Illumina's protocol and sequenced as 50-bp single reads on 12 lanes, generating an average of 34 million reads per sample. The adaptor sequence 5′-GATCGGAAGAGC-3′ was trimmed using FLEXBar (version 2.4), and reads were mapped to the mm9 mouse genome using STAR aligners (version 2.3.0e_r291)[63] with parameter --outFilterMismatchNmax 5.

The RNA-seq reads aligned to the genome were counted at each gene locus, and count values were transformed to reads per kilobase per million (RPKM) using the total number of uniquely mapping reads to all the genes and the length of each gene. For every tissue, a gene was called expressed if it had 5 RPKM or more in at least two of three samples. These genes were further analyzed. Analysis of differential gene expression was performed with edgeR[64], contrasting each of the targeted deletions of members of the miR-17~92 cluster (Δ17; Δ18; Δ19; Δ92; Δ17,18; and Δ17,18,92) against the wild-type condition.

Circos plots were generated using Circos software[37], and differentially expressed genes were selected using a 10% FDR cutoff. Predicted target sites were downloaded from TargetScan v6.2.

Enrichment of GO terms[65] in the biological processes category was calculated for genes differentially expressed ($|(\log_2(-\text{fold change})| \geq 0.26$ and FDR ≤ 1%) in each of the knockouts and in each of the tissues using the Bioconductor GOstats package[66], with all the genes expressed in each condition as background. Reported are GO terms filtered by size (between 15 and 250 genes) to focus on terms that were not too general or specific.

58. Rodríguez, C.I. *et al.* High-efficiency deleter mice show that FLPe is an alternative to Cre-*loxP*. *Nat. Genet.* **25**, 139–140 (2000).
59. Hafner, M. *et al.* Barcoded cDNA library preparation for small RNA profiling by next-generation sequencing. *Methods* **58**, 164–170 (2012).
60. Dobin, A. *et al.* STAR: ultrafast universal RNA-seq aligner. *Bioinformatics* **29**, 15–21 (2013).

doi:10.1038/ng.3321

61. Li, H. *et al.* The Sequence Alignment/Map format and SAMtools. *Bioinformatics* **25**, 2078–2079 (2009).
62. Liao, Y., Smyth, G.K. & Shi, W. featureCounts: an efficient general purpose program for assigning sequence reads to genomic features. *Bioinformatics* **30**, 923–930 (2014).
63. Dobin, A. *et al.* STAR: ultrafast universal RNA-seq aligner. *Bioinformatics* **29**, 15–21 (2013).
64. Robinson, M.D., McCarthy, D.J. & Smyth, G.K. edgeR: a Bioconductor package for differential expression analysis of digital gene expression data. *Bioinformatics* **26**, 139–140 (2010).
65. Ashburner, M. *et al.* Gene ontology: tool for the unification of biology. The Gene Ontology Consortium. *Nat. Genet.* **25**, 25–29 (2000).
66. Falcon, S. & Gentleman, R. Using GOstats to test gene lists for GO term association. *Bioinformatics* **23**, 257–258 (2007).